Chemical Science

ROYAL SOCIETY OF CHEMISTRY

EDGE ARTICLE

View Article Online
View Journal | View Issue

Cite this: *Chem. Sci.*, 2025, **16**, 15469

All publication charges for this article have been paid for by the Royal Society of Chemistry

Transmembrane nanogold energy transfer ruler enables *in situ* synchronized projecting of receptor dimerization–phosphorylation signaling†

Xingru Fang, Xurui Cao, Xiaotong Zhang, Qi Li, Wenwen Huang, Yu Zhang* and Honglin Liu *

Nanoscale dimerization geometries dictate transmembrane receptor phosphorylation dynamics, yet current methods fail to directly correlate spatial receptor organization with real-time phosphorylation states *in situ*. Receptor tyrosine kinase (RTK) activation, essential for cellular signaling, is dynamically controlled by dimerization at the nanoscale, but existing tools cannot simultaneously resolve spatial dimer configurations and phosphorylation activity. Here, we developed a transmembrane nanogold surface energy transfer ruler (T-Nanoruler) to enable *in situ* tracking of RTK activation. This system integrates extracellular DNA aptamers (ss-*n*-FAM) that program receptor dimerization spacer (0–8.6 nm) with intracellular gold nanoparticle–antibody conjugates (G_5@P-Met) targeting phosphorylated residues, creating a molecular ruler for nanoscale distance quantification. Using Met as a model, flow cytometry revealed distance-dependent quenching efficiencies that precisely matched phosphorylation levels validated by western blotting and scratch wound assays. Tight dimerization (0 nm spacer) maximized phosphorylation and cell migration, whereas extended configurations (8.6 nm spacer) suppressed activation. T-Nanoruler overcomes the limitations of FRET (limited detection range) and conventional *ex situ* methods (poor spatiotemporal resolution), establishing a versatile framework for probing spatial regulation across diverse RTK signaling systems. Our results established the first quantitative paradigm for synchronously mapping phosphorylation dynamics and dimerization geometries with nanometer precision, offering unprecedented insights into allosteric transmembrane signaling mechanisms.

Received 13th April 2025
Accepted 22nd July 2025

DOI: 10.1039/d5sc02717a

rsc.li/chemical-science

Introduction

Transmembrane protein phosphorylation, *e.g.*, receptor tyrosine kinase (RTK), serves as a central hub for cellular signaling, governing processes such as proliferation, survival, and migration by relaying extracellular cues to intracellular effectors.[1,2] Emerging studies demonstrate that the nanoscale spatial organization of RTKs directly governs their phosphorylation dynamics and functional outputs.[3–5] As a prototypical RTK, Met activates its tyrosine kinase domain upon HGF binding,[6,7] with precise dimerization levels dictating kinase activation thresholds and oncogenic signaling.[8,9] Compared to indirect detection approaches, directly targeting internal phosphorylation sites enables precise quantification of phosphorylation dynamics with site-specificity and high spatiotemporal resolution.[10] However, conventional techniques are unable to achieve simultaneous regulation of long-range transmembrane signal resolution and receptor spatial distribution while maintaining cellular integrity.[11,12] This technological bottleneck has forced reliance on indirect inferences to correlate receptor spatial distribution with functional phosphorylation states in intact cellular systems, which critically impedes the mechanistic elucidation of RTK-driven pathologies and hinders the development of spatially informed, targeted therapeutic strategies.

Current methodologies for analyzing protein phosphorylation fall into two categories: *ex situ* and *in situ* approaches. Conventional *ex situ* assays, including western blotting (WB), immunoprecipitation (IP), mass spectrometry, and ELISA,[13–15] face fundamental limitations in addressing contemporary demands of nanoscale spatial measurement. Firstly, spatial resolution is completely lost because cell lysis and homogenization disrupt the cellular distribution and prevent accurate reflection of membrane protein localization and levels.[16] Secondly, temporal resolution is also lost with only final static snapshots. *Ex situ* assays involve multiple steps (*e.g.*, fixation, permeabilization, antibody labeling), making results

Joint Research Center for Food Derived Functional Factors and Synthetic Biology of IHM, Anhui Provincial International Science and Technology Cooperation Base for Major Metabolic Diseases and Nutritional Interventions, China Light Industry Key Laboratory of Meat Microbial Control and Utilization, School of Food and Biological Engineering, Engineering Research Center of Bio-process, Ministry of Education, School of Chemistry and Chemical Engineering, Hefei University of Technology, Hefei 230601, P. R. China. E-mail: liuhonglin@mail.ustc.edu.cn; liuhonglin@hfut.edu.cn; zhangyu@hfut.edu.cn; 2020010130@mail.hfut.edu.cn

† Electronic supplementary information (ESI) available. See DOI: https://doi.org/10.1039/d5sc02717a

susceptible to interference.[17] Additionally, *in situ* assays, including immunofluorescence (IF) and Förster resonance energy transfer (FRET), partially address the above issues but encounter their own constraints.[18,19] IF is plagued by photobleaching artifacts and diffraction-limited spatial resolution; FRET's utility is restricted by its short detection range of usually less than 10 nm, preventing its use as an effective nanoruler for transmembrane signaling events.[20,21] Critically, FRET cannot bridge the long transmembrane distance separating extracellular dimerization interfaces from intracellular phosphorylation sites, forcing reliance on indirect validation *via* WB.[22,23] The existing gap in methodologies underscores the urgent need for developing novel *in situ* techniques to directly monitor protein phosphorylation levels at nanoscale resolution cells.

Recently, the novel optical nanoruler has risen as a fantastic tool to monitor molecular events on cell membranes.[24,25] Among these, nanometal surface energy transfer (NSET), pioneered by Jennings *et al.* in 2005, describes an energy transfer process between fluorescent dyes and nanoscale metal surfaces.[26] Through dipole-surface plasmon coupling,[27] NSET extends the detection range beyond 20 nm, overcoming the spatial constraints of FRET.[24,28] Unlike FRET, which is limited by dipole orientation sensitivity and endogenous background noise,[29,30] NSET operates *via* a $\frac{1}{R^4}$ distance-dependent decay profile, reducing orientation dependency and enhancing long-range efficiency.[26,31] Such long-range capability and low-background noise facilitate the precise correlation of transmembrane signaling events, including the direct resolution of dynamic interactions between extracellular receptor dimerization interfaces and intracellular kinase activation sites. By decoupling spatial resolution from molecular orientation, NSET provides a robust, non-invasive platform for nanoscale analysis, circumventing FRET's spatial limitations and structural artifacts of *ex situ* methods.

Here, we propose a novel transmembrane NSET nanoruler (T-Nanoruler) that synergizes two modular components: (1) extracellular DNA aptamers engineered to program receptor dimerization levels (0–8.6 nm *via* thymine spacers) and (2) intracellular GNP-antibody conjugates (G_5@P-Met) targeting phosphorylated tyrosine residues (Scheme 1). To rigorously exclude potential interference from the nanoparticle carriers (*e.g.*, nonspecific adsorption and background quenching effects), we employed PEG-functionalized GNPs (G_5@PEG) as a critical control group throughout the experiments.[32] This system operates as a bilayer-spanning nanoruler by tethering fluorophores (FAM) to the 5′ end of aptamers (ss-*n*-FAM) and G_5@P-Met to phosphorylation sites, T-Nanoruler establishes a quantifiable energy transfer pathway that directly links receptor spatial distribution to kinase activation levels.[33] Using Met as a model RTK, we demonstrate that controlled dimerization *via* ss-*n*-FAM induces distance-dependent autophosphorylation, with quenching efficiency (Φ) measured by flow cytometry (FCM) correlating precisely with phosphorylation levels validated by WB and functional migration assays.

The T-Nanoruler model resolves phosphorylation gradients across 0–8.6 nm receptor spacer adjustments, revealing that

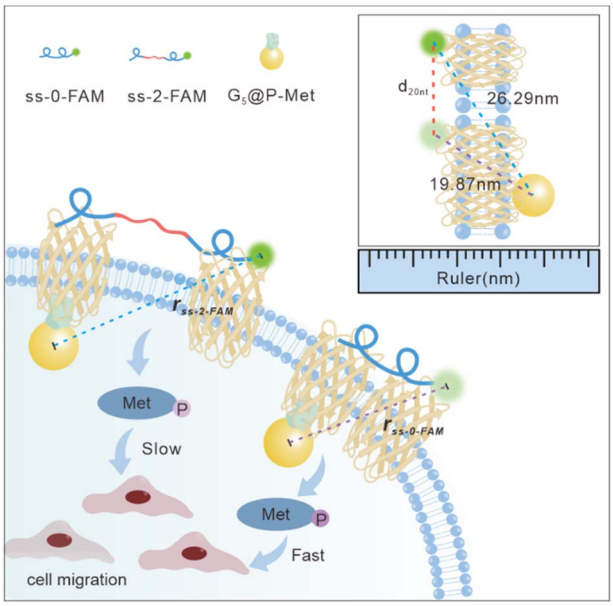

Scheme 1 Scheme of transmembrane NSET ruler (T-Nanoruler). The T-Nanoruler using FAM-labeled double Met aptamer DNA (ss-*n*-FAM) regulates receptor spacer (0–8.6 nm). In conjunction with G_5@P-Met to capture phosphorylation signals, FCM reflects that increased receptor spacer significantly reduces Met phosphorylation levels.

tighter dimerization (0 nm) enhances Met activation and cell migration compared to extended configurations (8.6 nm). This work pioneers a modular framework with potential to be extended for probing spatial regulation of RTK signaling, offering transformative potential for dissecting mechanisms of cancer metastasis, and drug resistance and designing topology-targeted kinase inhibitors.

Results

Synthesis and characterization of T-Nanoruler working components

HeLa cells with moderate Met expression were chosen as the model cell line. The selection ensures sufficient Met expression while preventing self-dimerization due to Met overexpression.[34] Laser confocal imaging demonstrated that HeLa cells were in optimal condition, exhibiting a highly intact cell nucleus (Fig. S1†). Saturation binding assays with ss-*n*-FAM revealed a concentration-dependent interaction. FCM analysis showed that both ss-0-FAM (no spacer) and ss-2-FAM (20T spacer) reached saturation at 400 nM (Fig. 1A and B). Dissociation constants (K_d) calculated from nonlinear regression were 48.43 nM (ss-0-FAM) and 32.15 nM (ss-2-FAM) (Fig. S2†), indicating T-spacer insertion minimally impacted aptamer affinity. Subsequently, the time-course experiment identified 15 min as the optimal incubation time for ss-*n*-FAM binding (Fig. 1C and D). To construct the energy acceptor (G_5@P-Met), G_5 was synthesized and conjugated to anti-P-Met through electrostatic adsorption. Transmission electron microscopy (TEM) images showed that the synthesized particles had an average diameter

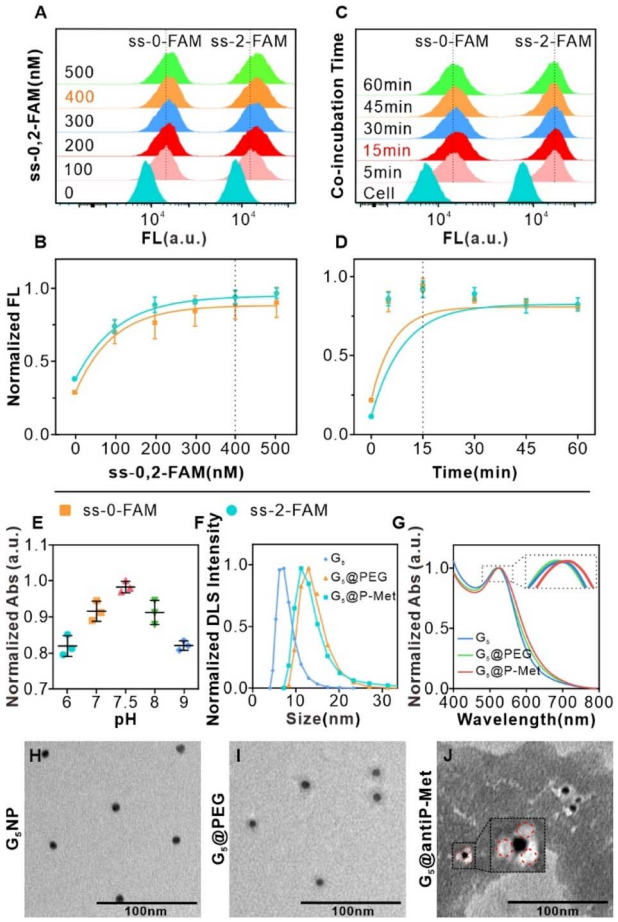

Fig. 1 Synthesis and characterization of T-Nanoruler working components. (A and B) Saturated binding concentration analysis of the ss-0, 2-FAM aptamers to Met receptors on HeLa cells. The FCM charts indicated ss-0, 2-FAM at 0, 100, 200, 300, 400, and 500 nM from bottom to top in (A), respectively. (C and D) Optimal co-incubation time of ss-*n*-FAM aptamers and Met receptors on HeLa cells. The FCM charts indicated native HeLa cells and cells saturated with ss-*n*-FAM for about 5, 15, 30, 45, and 60 min from bottom to top in (C), respectively. (E) The hydrodynamic diameters of G_5NP, G_5@PEG, and G_5@P-Met by DLS measurements, respectively. (F) Normalized absorbance of G_5@P-Met conjugates at varied pH values. (G) UV-VIS absorption spectra of G_5 (blue line), G_5@PEG (orange line), and G_5@P-Met (green line). (H–J) TEM images of G_5, G_5@PEG, and G_5@P-Met, respectively. The red circle in (J) indicates the coupling of anti-P-Met on G_5. Scale bar: 100 nm.

of 5.4 nm, with uniform size and good dispersion (Fig. 1H and S3). Since the antibody is amphoteric, the binding to GNP surfaces is pH-dependent.[35] Therefore, we investigated the impact of pH, finding optimal coupling efficiency at pH 7.5 (Fig. 1E). Additionally, control nanoparticles (G_5@PEG) were prepared by functionalizing G_5 with thiolate polyethylene glycol (PEG) *via* Au–S bonds. Successful conjugation was validated by dynamic light scattering (DLS) (Fig. 1F), UV-Vis spectroscopy (Fig. 1G), zeta potential (Fig. S4†), and TEM imaging (Fig. 1I and J). Notably, TEM-negative staining revealed antibody coronas around the G_5 surface of G_5@P-Met, with an average size increased to 12 nm (Fig. S3†).

Validation of fluorescence signal stability under cellular permeabilization

To enable intracellular delivery of G_5@P-Met and G_5@PEG, we first labeled cells with saturated concentrations of ss-*n*-FAM. After confirming effective binding, we treated the cells with paraformaldehyde (PFA) and Triton X-100, which serve to permeabilize the cell membranes, thereby facilitating the internalization of the nanoparticles. To determine whether these permeabilization agents could interfere with the FL of the labeled cells, we performed confocal microscopy (Fig. 2A–I) and FCM analyses (Fig. 2J and K). Our results showed that neither PFA nor Triton X-100 significantly affected fluorescence intensity, indicating negligible FL interference. Moreover, no

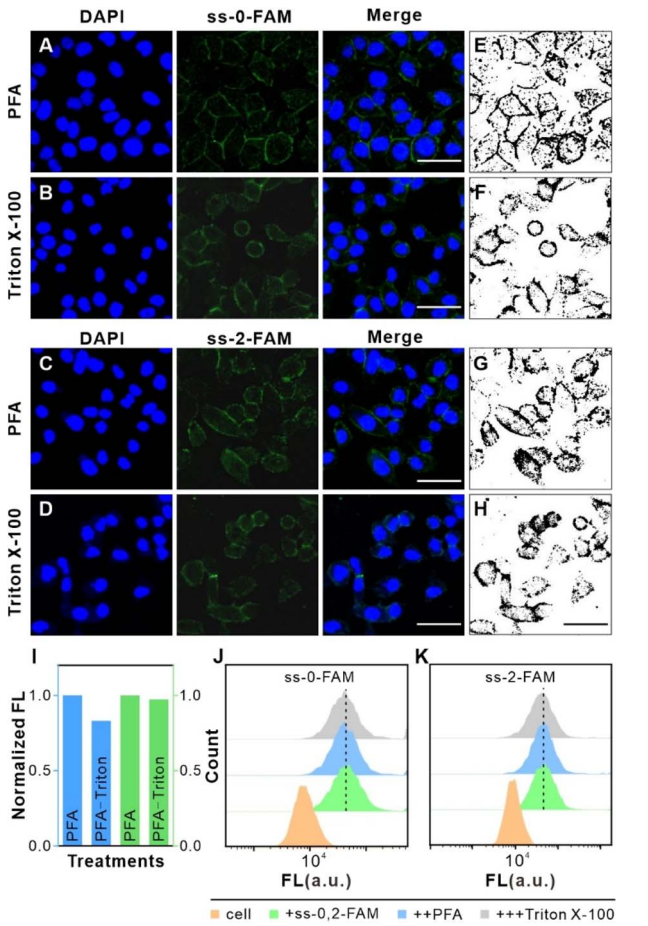

Fig. 2 The effects of PFA and Triton X-100 on the FL of saturated ss-*n*-FAM. (A–D) The confocal imaging analysis of HeLa cells. Specifically, (A and B) HeLa cells stained with saturated ss-0-FAM and DAPI. The images show DAPI (left), ss-0-FAM (middle), and merge (right) imaging after treatment with PFA in (A) and Triton X-100 in (B), respectively. Scale bar: 50 μm. (C and D) HeLa cells stained with saturated ss-2-FAM and DAPI. The images show DAPI (left), ss-2-FAM (middle), and merge (right) imaging after treatment with PFA in (C) and Triton X-100 in (D). Scale bar: 50 μm. (E–H) Grey-scale images of FAM FL in (A–D) cells were estimated using Image J software. Scale bar: 50 μm. (I) Normalized grey values for (E–H) were calculated using Image J software. (J and K) FL changes in HeLa cells containing saturated ss-*n*-FAM after treatment with PFA and Triton X-100 were measured by FCM.

changes in native cell fluorescence were observed, ensuring the reliability of these findings (Fig. S5†).

Quantitative correlation between T-Nanoruler energy transfer efficiency and receptor dimerization distance

We employed T-Nanoruler to track Met monomer dimerization events within cells. FCM analysis revealed comparable FL between cells bound with saturated ss-0-FAM and ss-2-FAM, respectively (Fig. 3A–C). The introduction of the non-targeted control G_5@PEG induced similar minor FL changes in both groups. In contrast, when G_5@P-Met was introduced, the FL of ss-0-FAM decreased significantly compared to ss-2-FAM (Fig. 3D and S6†). To further validate the model's accuracy, we introduced the ss-1-FAM variant with a 10T spacer to examine its distance-gradient effect. The binding properties of this variant with HeLa cells (400 nM, 15 min) were consistent with those of the ss-0-FAM and ss-2-FAM systems (Fig. S7†). The results showed that the decrease in FL induced by G_5@P-Met was precisely located between ss-0-FAM and ss-2-FAM (Fig. S8†). In summary, the spacer length of ss-*n*-FAM directly and quantitatively determined the FL quenching gradient by regulating Met phosphorylation levels.

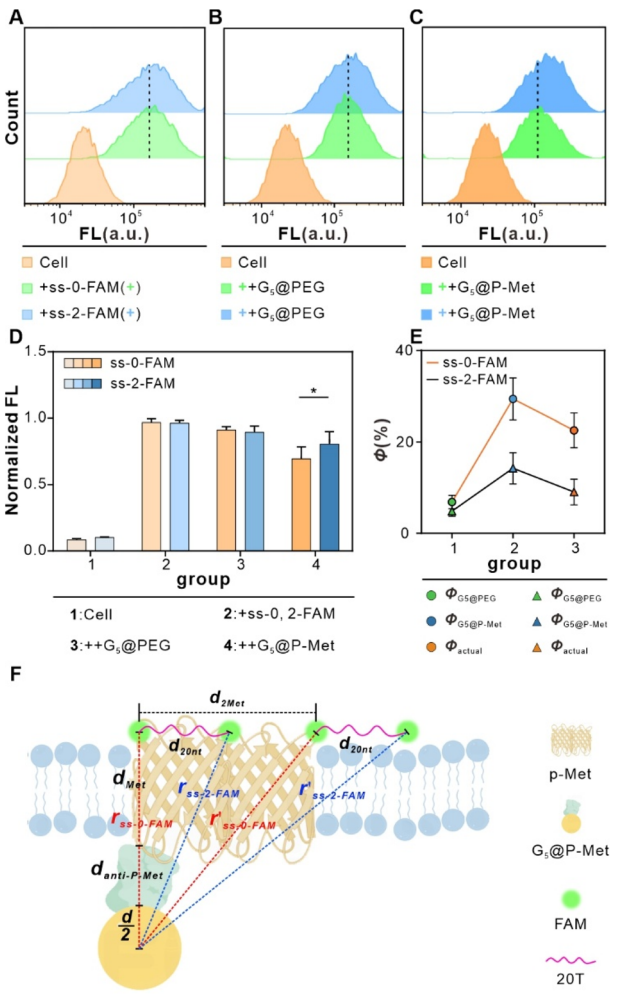

Fig. 3 *In situ* tracking of Met phosphorylation levels by T-Nanoruler through experiments. (A) FCM analysis of cells incubated with saturated ss-*n*-FAM. (B) FCM analysis of cells incubated with saturated ss-*n*-FAM followed by G_5@PEG, respectively. (C) FCM analysis of cells incubated with saturated ss-*n*-FAM followed by G_5@P-Met, respectively. (D) Normalized FL for (A)–(C). Data are expressed as means ± SD (*$P < 0.05$). (E) The Φ of cells in the ss-0-FAM group and the ss-2-FAM group. (F) Geometric modeling of single-size G_5–FAM pairs of straight-line distances in T-Nanoruler system.

We then calculated the Φ using eqn (1) and (2) based on FL change in HeLa cells after binding ss-*n*-FAM (donors) to G_5@PEG (Φ_{PEG}) or G_5@P-Met ($\Phi_{P\text{-}Met}$) (acceptors):

$$\Phi_{PEG} = \frac{I_0 - I_{PEG}}{I_0} \quad (1)$$

$$\Phi_{P\text{-}Met} = \frac{I_0 - I_{P\text{-}Met}}{I_0} \quad (2)$$

where I_0 is the cell FL of ss-*n*-FAM minus native cells' autofluorescence; I_{PEG} represents the cell FL of ss-*n*-FAM with G_5@PEG after subtracting native cells' autofluorescence, while $I_{P\text{-}Met}$ represents the cell FL of ss-*n*-FAM with G_5@P-Met after the same subtraction. As shown in Fig. 3E, $\Phi_{PEG} = 6.85\%$ and $\Phi_{P\text{-}Met} = 29.39\%$ in cells coupled to ss-0-FAM; $\Phi_{PEG} = 4.84\%$ and $\Phi_{P\text{-}Met} = 14.14\%$ in cells coupled to ss-2-FAM. Specifically, the Φ_{PEG} values primarily arose from G_5's intrinsic internal filtering effect. To isolate the influence of this background, G_5@PEG served as the control. Therefore, after subtracting Φ_{PEG}, the Φ_{actual}=22.54% in cells for ss-0-FAM and Φ_{actual}=9.3% in cells for ss-2-FAM. For the ss-1-FAM group, the Φ_{actual} was calculated using the same method and found to be 13.7% (Fig. S9†). Therefore, the Φ_{actual} shows a gradient decrease across the ss-0-FAM, ss-1-FAM, and ss-2-FAM groups (from 22.54% to 13.7% and then to 9.3%), which highly corresponds with the theoretical distance model. However, the difference in Φ_{actual} between ss-1-FAM (13.7%) and ss-2-FAM (9.3%) is relatively small. Therefore, in the subsequent studies, we still chose to use 0T (ss-0) and 20T (ss-2) spacers for comparative research.

Next, we further observed the quenching of ss-0-FAM and ss-2-FAM at the cellular level using laser confocal imaging. As shown in Fig. S10,† in the G_5@PEG group (without targeting ligand), the quenching effect of both probes was not significant; however, after adding G_5@P-Met, significant FAM fluorescence quenching was observed in both probe groups, with the ss-0-FAM group showing particularly pronounced quenching. These results further support the molecular proximity-induced cellular-level quenching mechanism.

The T-Nanoruler model describes energy transfer between a point dipole (donor, FAM) and a surface dipole (acceptor, G_5), with the latter modeled as an infinite array of point dipoles.[36,37]

Therefore, the relationship between Φ and donor–acceptor separation distance (r) is given by eqn (3):[26]

$$\Phi = \frac{1}{1 + \left(\frac{r}{r_0}\right)^4} \quad (3)$$

where r_0 is the surface energy transfer radius, determined to be 14.97 nm for the G_5–FAM pair within the cellular system.[38] The r represents the distance from FAM dye to the surface of G_5NPs.

Based on the measured Φ values, the r was calculated as $r_{\text{ss-0-FAM}} = 19.82$ nm and $r_{\text{ss-2-FAM}} = 26.42$ nm, respectively.

As depicted in Fig. 3F, we treated the Met protein dimer as a single entity and calculated the theoretical separation distance to the donor–acceptor pair (r'). Due to uncertainty regarding the binding site of ss-n-FAM on the Met surface, we computed a range of separation distances corresponding to the nearest (left) and farthest (right) binding sites.

In the previous section, the average length of G_5@P-Met was 12 nm. Consequently, the sum of the G_5 radius $\left(\frac{d}{2}\right)$ and the anti-P-Met ($d_{\text{anti-P-Met}}$) was estimated to be 9.3 nm (d_1). The Stokes radius of Met was calculated using eqn (4):[39]

$$R_{\text{Stokes}} = 66 \times 10^{-3} M^{\frac{1}{3}} \quad (4)$$

where M is the molecular mass of the protein. For a Met monomer with a mass of 190 kDa, the Stokes radius is approximately 3.8 nm. Therefore, the whole length of Met is 7.6 nm (d_{Met}). Subsequently, $r'_{\text{N-ss-0-FAM}}$ was determined using eqn (5), while $r'_{\text{F-ss-0-FAM}}$, $r'_{\text{N-ss-2-FAM}}$, and $r'_{\text{F-ss-2-FAM}}$ were calculated using eqn (6) based on the Pythagorean theorem:

$$r'_1 = \left(\frac{d}{2} + d_{\text{anti-P-Met}}\right) + d_{\text{Met}} \quad (5)$$

$$r'_2 = r'^{2}_{\text{N-ss-0-FAM}} + d^{2}_{\text{NF}} \quad (6)$$

where d_{NF} represents the distance between the receptor's farthest and nearest binding sites. Each base of the oligonucleotide is approximately 0.43 nm in length. Therefore, the theoretical range of $r'_{\text{ss-0-FAM}}$ is estimated between 16.9 nm and 22.73 nm, and that of $r'_{\text{ss-2-FAM}}$ is between 18.96 nm and 29.19 nm. Since r indicates the distance from the fluorescent dye to the surface of the GNP core, after subtracting the GNP radius (2.7 nm), the theoretical values are adjusted to 14.2–20.03 nm (ss-0-FAM) and 16.26–26.49 nm (ss-2-FAM). Consequently, the experimentally measured values, $r_{\text{ss-0-FAM}}$ (19.82 nm) and $r_{\text{ss-2-FAM}}$ (26.42 nm) fall within the theoretical ranges.

Precision calibration of T-Nanoruler: resolving conformational flexibility and signal specificity

Building on the confirmation that the T-Nanoruler model can accurately establish the correlation between receptor dimerization distances and phosphorylation levels. We further investigated the impact of the single-stranded DNA (ssDNA) scaffold's flexibility and monovalent receptor binding on the model's accuracy.

Due to its inherent flexibility, the 20T ssDNA spacer may cause conformational fluctuations, resulting in distance deviations that could affect the precision of experimental outcomes. To precisely quantify the measurement bias caused by conformational fluctuations of the ssDNA spacer, we introduced a rigid variant containing a 20 bp AT double-stranded spacer region, ds-2-FAM, for detailed study. As shown in Fig. 4A and B, the saturation binding parameters for the double-stranded variant ds-2-FAM were 400 nM and 15 minutes. Subsequent quenching experiments indicated that the actual quenching

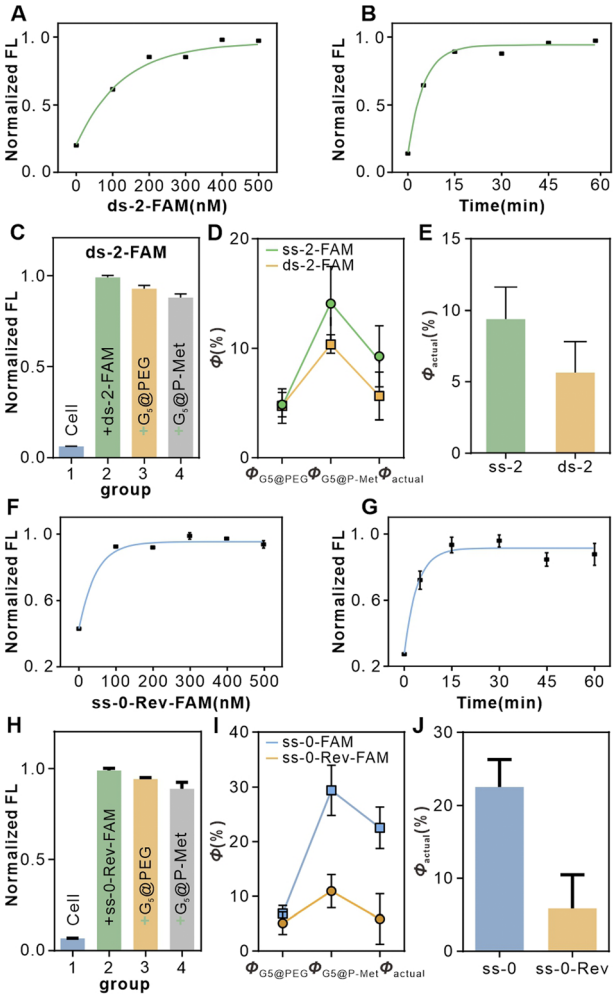

Fig. 4 Validation of the accuracy of the T-Nanoruler model. (A) Saturated binding concentration analysis of the ds-2-FAM aptamers to Met receptors on HeLa cells. (B) Optimal co-incubation time of ds-2-FAM aptamers and Met receptors on HeLa cells. (C) Flow cytometry data analysis of quenching experiments after incubation of cells with ds-2-FAM aptamers at saturation concentration. (D) The Φ of cells in the ss-2-FAM and ds-2-FAM groups. (E) Statistics of Φ_{actual} in the ss-2-FAM and ds-2-FAM groups in (D). (F) Saturated binding concentration analysis of the ss-0-Rev-FAM aptamers to Met receptors on HeLa cells. (G) Optimal co-incubation time of ss-0-Rev-FAM aptamers and Met receptors on HeLa cells. (H) Flow cytometry data analysis of quenching experiments after incubation of cells with ss-0-Rev-FAM aptamers at saturation concentration. (I) The Φ of cells in the ss-0 FAM and ss-0-Rev-FAM groups. (J) Statistics of Φ_{actual} in the ss-0 FAM and ss-0-Rev-FAM groups in (I).

efficiency of ds-2-FAM ($\Phi_{\text{actual}} = 5.64\%$) was lower than that of ss-2-FAM ($\Phi_{\text{actual}} = 9.3\%$) (Fig. 4C and D). This result aligns with the rigid extension characteristics of double-stranded DNA. It is noteworthy that the 3.66% difference in quenching efficiency between the two remains relatively low (Fig. 4E), which fully confirms that the bias introduced by the flexibility of the single strand is controllable within this model.

Previous studies focused on the ss-n series aptamers, all of which were activating variants capable of inducing Met dimerization. However, investigating monovalent Met aptamer

variants helps clarify the central role dimerization plays in signal activation. To this end, we designed ss-0-Rev-FAM containing the SL1 sequence (monomeric Met aptamer) and its reverse sequence (SL1 reverse) as a negative control. This sequence can bind only monovalent Met and cannot induce dimerization (SL1 reverse sequence has been validated as a negative control). First, we optimized the binding conditions for ss-0-Rev-FAM, finding a saturation concentration of 300 nM and an optimal incubation time of 30 minutes (Fig. 4F and G). Subsequent quenching experiments revealed that the actual quenching efficiency of ss-0-Rev-FAM (Φ_{actual} = 5.26%) was significantly lower than that of the ss-0-FAM group (Φ_{actual} = 22.54%) (Fig. 4H and I). Although the binding of a single aptamer may slightly influence protein activation, it cannot induce dimerization, resulting in markedly lower quenching efficiency than that of ss-0-FAM (Fig. 4J). This result further confirms that the significant quenching effect observed in the experimental group (ss-0-FAM) is primarily driven by the specific binding of the Met aptamer and the dimerization it induces.

Biological validation of dimerization distance-dependent signaling

Autophosphorylation of the Met receptor acts as a molecular switch for downstream proliferation and migration signaling pathways,[40] and its activation level is gradient-regulated through dimerization diatance precisely programmed by T-Nanoruler. Since the FAM fluorophore has no significant impact on this part of the experiment, we used ss-0 and ss-2 aptamers (collectively referred to as ss-*n*) for subsequent functional analysis. WB results showed that the Met phosphorylation level in HeLa cells treated with ss-*n* was significantly higher than that in the untreated group, and the induction efficacy of ss-0 was obviously stronger than that of ss-2, confirming the distance-dependent regulation of phosphorylation efficiency (Fig. 5A$_I$ and B).

The differences in receptor phosphorylation levels caused by different treatments directly regulate cellular functions such as migration and proliferation (Fig. 5A$_{II}$).[41] We explored the changes in the proliferation rate of HeLa cells under different treatments using the CCK-8 assay. As shown in Fig. 5C, both ss-0 and ss-2 treatment groups significantly promoted the proliferation of HeLa cells, with the ss-0 group being obviously superior to the ss-2 group. In contrast, the control sequences ds-2 and ss-0-Rev did not induce significant changes (Fig. S11†). Furthermore, scratch wound assays revealed that the cell migration rates in the ss-0 and ss-2 treatment groups increased to 54.16% and 34.23% respectively (15.4% in the control group) (Fig. 5D and E), while the ds-2 and ss-0-Rev groups still had no significant effects (Fig. S12†). This functional difference is directly attributed to the Met phosphorylation gradient regulated by ss-*n* through dimerization spacing, which is consistent with previously reported results.[40]

To further rule out non-specific effects, we investigated the cell migration of the Met-negative cell line SH-SY5Y under different treatments.[42] The results showed that there was no

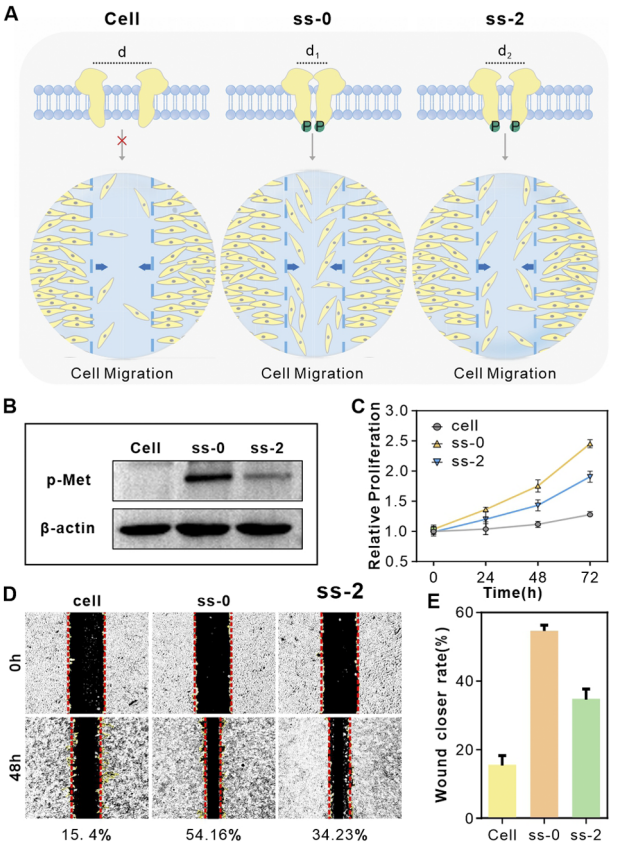

Fig. 5 The ss-0, 2-FAM regulate cellular receptors. (A) Schematic representation of phosphorylation of downstream proteins and the cell migration rate of HeLa cells after different treatments. From left to right: cell, treated with ss-0, and treated with ss-2. (B) Western blot analysis of the activation of Met by ss-*n* in HeLa cells. (C) ss-*n* treatment modulates proliferation of HeLa cells assessed by CCK-8 assay. (D) ss-*n* regulated wound healing, imaged at 0 and 48 hours. ((1) cell; (2) treated with ss-0; (3) treated with ss-2). The efficiency of wound healing reflects the ability of cells to migrate. (E) Statistical analysis of relative wound healing rates.

significant difference in the migration rate of SH-SY5Y cells under different treatments (Fig. S13†). This is because SH-SY5Y cells hardly express the Met receptor, so the ss-*n* components have no regulatory effect on these cells. In summary, T-Nanoruler achieves directional regulation of Met phosphorylation and downstream cellular behaviors by precisely controlling the spatial conformation of receptor dimerization.

Discussion

The development of the T-Nanoruler strategy addresses a critical gap in the ability to track RTK phosphorylation levels *in situ* under controlled spatial distributions. Conventional methods such as western blotting disrupt native cellular architectures, while FRET-based approaches are limited by their short detection range (<10 nm). By integrating programmable DNA aptamers with tunable lengths and gold nanoparticle–antibody conjugates, T-Nanoruler achieves *in situ* tracking of different phosphorylation levels, significantly surpassing traditional

techniques. The observed distance-dependent regulation of Met phosphorylation directly correlates with cellular migration rate, validating the hypothesis that receptor dimerization distance governs signaling efficacy.

A critical advantage of T-Nanoruler lies in its modular design. The correlation between Φ values and western blot data confirms its reliability. Unlike FRET, which is constrained by dipole orientation,[24] T-Nanoruler leverages the broad energy transfer range of gold nanoparticles, enabling transmembrane tracking of phosphorylation events. The modular aptamer design opens possibilities for adaptation to other RTKs (*e.g.*, EGFR, HER2) with further optimization. These findings expand upon prior NSET applications by the dual-component system capable of simultaneous spatial manipulation and *in situ* tracking. While the T-Nanoruler model assumes a flat and homogeneous membrane, real biological membranes exhibit complexities such as curvature, receptor clustering, and lipid microdomains. Although this simplification may introduce uncertainties in distance quantification, its strength lies in establishing a tractable mathematical framework between intermolecular distance and Φ by excluding secondary variables. This approach significantly reduces experimental and analytical complexity, enabling practical *in situ* nanoscale measurements in living cells.[43] Future studies will incorporate membrane topology mapping to further calibrate environmental perturbations. However, certain limitations warrant consideration. The current model relies on fixed-cell imaging, which precludes dynamic tracking in live systems. Additionally, while the modular aptamer design permits adaptation to other RTKs, variations in aptamer binding affinities may necessitate optimization for broader applicability. Future studies could integrate time-lapse imaging or multiplexed probes to resolve spatiotemporal phosphorylation patterns in cells.

In summary, we presented T-Nanoruler as a transformative strategy for investigating receptor (exemplified by Met) phosphorylation levels at nanoscale resolution. By coupling spatially programmable DNA aptamers with NSET, this strategy enables *in situ* correlation of receptor dimerization distances with phosphorylation levels and downstream cellular behaviors. The method's modular architecture and compatibility with flow cytometry position it as a versatile tool for studying spatial regulation in cancer biology, drug discovery, and receptor engineering.

Data availability

Details of methods, experimental procedures, and additional data are available in the ESI.† Further information and requests for resources should be directed to and will be fulfilled by the lead contact, Honglin Liu (liuhonglin@mail.ustc.edu.cn).

Author contributions

Xingru Fang: investigation, conceptualization, methodology, formal analysis, data curation, visualization, writing–original draft, review, and editing. Xurui Cao: investigation. Xiaotong Zhang: investigation. Qi Li: investigation. Wenwen Huang: investigation. Yu Zhang: conceptualization, methodology, formal analysis, data curation, resources, writing – review, editing, and supervision. Honglin Liu: conceptualization, methodology, formal analysis, data curation, resources, writing – review, editing, and supervision.

Conflicts of interest

There are no conflicts to declare.

Acknowledgements

This work was funded by the Yangtze River Delta Science and Technology Innovation Community Joint Basic Research Project (Grant Number: 2024CSJZN1200), the National Natural Science Foundation of China (Grant Numbers: 22474030 and 22274034), the Fundamental Research Funds for the Central Universities of China (Grant Numbers: PA2023GDGP0040 and PA2024GDGP0037), and the China Postdoctoral Science Foundation (Grant Numbers: 2025M771106).

References

1 R. Trenker and N. Jura, Receptor tyrosine kinase activation: From the ligand perspective, *Curr. Opin. Cell Biol.*, 2020, **63**, 174–185.
2 L. Chen, W. M. Marsiglia, H. Chen, J. Katigbak, H. Erdjument-Bromage, D. J. Kemble, L. Fu, J. Ma, G. Sun, Y. Zhang, G. Liang, T. A. Neubert, X. Li, N. J. Traaseth and M. Mohammadi, Molecular basis for receptor tyrosine kinase A-loop tyrosine transphosphorylation, *Nat. Chem. Biol.*, 2020, **16**, 267–277.
3 A. Comberlato, M. M. Koga, S. Nüssing, I. A. Parish and M. M. C. Bastings, Spatially controlled activation of Toll-like receptor 9 with DNA-based nanomaterials, *Nano Lett.*, 2022, **22**, 2506–2513.
4 J. B. Casaletto and A. I. McClatchey, Spatial regulation of receptor tyrosine kinases in development and cancer, *Nat. Rev. Cancer*, 2012, **12**, 387–400.
5 Y. Chen, K. Morihiro, Y. Nemoto, A. Ichimura, R. U. Sando and A. Okamoto, Selective inhibition of cancer cell migration using a pH-responsive nucleobase-modified DNA aptamer, *Chem. Sci.*, 2024, **15**, 17097.
6 S. L. Organ and M.-S. Tsao, An overview of the c-MET signaling pathway, *Ther. Adv. Med. Oncol.*, 2011, **3**, S7–S19.
7 L. Trusolino, A. Bertotti and P. M. Comoglio, MET signaling: Principles and functions in development, organ regeneration and cancer, *Nat. Rev. Mol. Cell Biol.*, 2010, **11**, 834–848.
8 S. B. de Lara, S. Kemmer, I. Biermayer, S. Feiler, A. Vlasov, L. A. D'Alessandro, B. Helm, C. Mölders, Y. Dieter, A. Ghallab, J. G. Hengstler, C. Körner, M. Matz-Soja, C. Götz, G. Damm, K. Hoffmann, D. Seehofer, T. Berg, M. Schilling, J. Timmer and U. Klingmüller, Basal MET phosphorylation is an indicator of hepatocyte dysregulation in liver disease, *Mol. Syst. Biol.*, 2024, **20**, 187–216.

9 H. Geng, S. Zhi, X. Zhou, Y. Yan, G. Zhang, S. Dai, S. Lv and S. Bi, Self-Powered Engineering of Cell Membrane Receptors to On-Demand Regulate Cellular Behaviors, *Nano Lett.*, 2024, **24**(26), 7895–7902.

10 H. Li, M. Wang, T. Shi, S. Yang, J. Zhang, H.-H. Wang and Z. Nie, A DNA-mediated chemically induced dimerization (D-CID) nanodevice for nongenetic receptor engineering to control cell behavior, *Angew. Chem., Int. Ed.*, 2018, **57**, 10226–10230.

11 Y. Li, X. Zhang, W. Pan, N. Li and B. Tang, A nongenetic proximity-induced FRET strategy based on DNA tetrahedron for visualizing the receptor dimerization, *Anal. Chem.*, 2020, **92**, 11921–11930.

12 C. Simonneau, B. Leclercq, A. Mougel, E. Adriaenssens, C. Paquet, L. Raibaut, N. Ollivier, H. Drobecq, J. Marcoux, S. Cianferani, D. Tulasne, H. de Jonge, O. Melnyk and J. Vicogne, Semi-synthesis of a HGF/SF kringle one (K1) domain scaffold generates a potent *in vivo* MET receptor agonist, *Chem. Sci.*, 2015, **6**, 2110–2121.

13 L. Wang, H. Liang, J. Sun, Y. Liu, J. Li, J. Li, J. Li and H. Yang, Bispecific aptamer induced artificial protein-pairing: A strategy for selective inhibition of receptor function, *J. Am. Chem. Soc.*, 2019, **141**, 12673–12681.

14 M. Wang, D. Yang, Q. Lu, L. Liu, Z. Cai, Y. Wang, H.-H. Wang, P. Wang and Z. Nie, Spatially reprogramed receptor organization to switch cell behavior using a DNA origami-templated aptamer nanoarray, *Nano Lett.*, 2022, **22**, 8445–8454.

15 R. Ueki, A. Ueki, N. Kanda and S. Sando, Oligonucleotide-based mimetics of hepatocyte growth factor, *Angew. Chem.*, 2016, **128**, 589–592.

16 C. F. Moh, S. L. Siedlak, M. Tabaton, G. Perry, R. J. Castellani and M. A. Smith, Paraffin-embedded tissue (PET) blot method: Application to Alzheimer disease, *J. Neurosci. Methods*, 2010, **190**, 244–247.

17 M. Mishra, S. Tiwari and A. V. Gomes, Protein purification and analysis: Next generation Western blotting techniques, *Expert Rev. Proteomics*, 2017, **14**, 1037–1053.

18 I. Mayer, T. Karimian, K. Gordiyenko, A. Angelin, R. Kumar, M. Hirtz, R. Mikut, M. Reischl, J. Stegmaier, L. Zhou, R. Ma, G. U. Nienhaus, K. S. Rabe, P. Lanzerstorfer, C. M. Domínguez and C. M. Niemeyer, Surface-patterned DNA origami rulers reveal nanoscale distance dependency of the epidermal growth factor receptor activation, *Nano Lett.*, 2024, **24**, 1611–1619.

19 W. Yang, H. Nan, Z. Xu, Z. Huang, S. Chen, J. Li, J. Li and H. Yang, DNA-templated glycan labeling for monitoring receptor spatial distribution in living cells, *Anal. Chem.*, 2021, **93**, 12265–12272.

20 L. Wang, W. Li, J. Sun, S.-Y. Zhang, S. Yang, J. Li, J. Li and H.-H. Yang, Imaging of receptor dimers in zebrafish and living cells *via* aptamer recognition and proximity-induced hybridization chain reaction, *Anal. Chem.*, 2018, **90**, 14433–14438.

21 T. Förster, Zwischenmolekulare energiewanderung und fluoreszenz, *Ann. Phys.*, 1948, **437**, 55–75.

22 Y. Wang, Y. Xiong, L. Song, S. He, F. Yao, Y. Wu, K. Shi and L. He, Spatial control of receptor dimerization using programmable DNA nanobridge, *Biomacromolecules*, 2023, **24**, 3228–3236.

23 H. Liang, S. Chen, P. Li, L. Wang, J. Li, J. Li, H.-H. Yang and W. Tan, Nongenetic approach for imaging protein dimerization by aptamer recognition and proximity-induced DNA assembly, *J. Am. Chem. Soc.*, 2018, **140**, 4186–4190.

24 Y. Zhang, X. Fang, W. Huang, Q. Li, F. Hu and H. Liu, Record resolution of nanometal surface energy transfer optical nanoruler projects 3D spatial configuration of aptamers on a living cell membrane, *Nano Lett.*, 2023, **23**, 11968–11974.

25 Y. Zhang, M. Su, X. Fang, W. Huang, H. Jiang, Q. Li, N. Hussain, M. Ye, H. Liu and W. Tan, Single-nucleobase resolution of a surface energy transfer nanoruler for *in situ* measurement of aptamer binding at the receptor subunit level in living cells, *Chem. Sci.*, 2023, **14**, 9560.

26 C. S. Yun, A. Javier, T. Jennings, M. Fisher, S. Hira, S. Peterson, B. Hopkins, N. O. Reich and G. F. Strouse, Nanometal surface energy transfer in optical rulers, breaking the FRET barrier, *J. Am. Chem. Soc.*, 2005, **127**, 3115–3119.

27 C. Chen and N. Hildebrandt, Resonance energy transfer to gold nanoparticles: NSET defeats FRET, *TrAC, Trends Anal. Chem.*, 2020, **123**, 115748.

28 Y. Chen, M. B. O'Donoghue, Y.-F. Huang, H. Kang, J. A. Phillips, X. Chen, M.-C. Estevez, C. J. Yang and W. Tan, A surface energy transfer nanoruler for measuring binding site distances on live cell surfaces, *J. Am. Chem. Soc.*, 2010, **132**, 16559–16570.

29 E. A. Jares-Erijman and T. M. Jovin, FRET imaging, *Nat. Biotechnol.*, 2003, **21**, 1387–1395.

30 P. R. Selvin, The renaissance of fluorescence resonance energy transfer, *Nat. Struct. Biol.*, 2000, **7**, 730–734.

31 P. C. Ray, Z. Fan, R. A. Crouch, S. S. Sinha and A. Pramanik, Nanoscopic optical rulers beyond the FRET distance limit: Fundamentals and applications, *Chem. Soc. Rev.*, 2014, **43**, 6370–6404.

32 X. Li, V. Vemireddy, Q. Cai, H. Xiong, P. Kang, X. Li, M. Giannotta, H. N. Hayenga, E. Pan, S. R. Sirsi, C. Mateo, D. Kleinfeld, C. Greene, M. Campbell, E. Dejana, R. Bachoo and Z. Qin, Reversibly Modulating the Blood-Brain Barrier by Laser Stimulation of Molecular-Targeted Nanoparticles, *Nano Lett.*, 2021, **21**(22), 9805–9815.

33 M. P. Singh, T. L. Jennings and G. F. Strouse, Tracking spatial disorder in an optical ruler by time-resolved NSET, *J. Phys. Chem. B*, 2009, **113**, 552–558.

34 D. E. Hammond, S. Urbé, G. F. Vande Woude and M. J. Clague, Down-regulation of MET, the receptor for hepatocyte growth factor, *Oncogene*, 2001, **20**, 2761–2770.

35 G. Ruiz, K. Tripathi, S. Okyem and J. D. Driskell, pH impacts the orientation of antibody adsorbed onto gold nanoparticles, *Bioconjugate Chem.*, 2019, **30**, 1182–1191.

36 C. Chen, C. Midelet, S. Bhuckory, N. Hildebrandt and M. H. V. Werts, Nanosurface energy transfer from long-

lifetime terbium donors to gold nanoparticles, *J. Phys. Chem. C*, 2018, **122**, 17566–17574.

37 C. Chen and N. Hildebrandt, Resonance energy transfer to gold nanoparticles: NSET defeats FRET, *TrAC, Trends Anal. Chem.*, 2020, **123**, 115748.

38 W. Huang, Y. Zhang, X. Fang, Q. Li and H. Liu, Single-nucleobase-resolved nanoruler determines the surface energy transfer radius on the living cell membrane, *Anal. Chem.*, 2024, **96**, 5274–5281.

39 G. M. Rothe, Determination of molecular mass, Stokes' radius, frictional coefficient and isomer-type of non-denatured proteins by time-dependent pore gradient gel electrophoresis, *Electrophoresis*, 1988, **9**, 307–316.

40 M. Wang, F. He, H. Li, S. Yang, J. Zhang, P. Ghosh, H.-H. Wang and Z. Nie, Near-infrared light-activated DNA-agonist nanodevice for nongenetically and remotely controlled cellular signaling and behaviors in live animals, *Nano Lett.*, 2019, **19**, 2603–2613.

41 K. Ito, K. Sakai, Y. Suzuki, N. Ozawa, T. Hatta, T. Natsume, K. Matsumoto and H. Suga, Artificial human Met agonists based on macrocycle scaffolds, *Nat. Commun.*, 2015, **6**, 6373.

42 Q. Zou, B. Du, X. Wang, H. Wang, J. Sun, X. Yang, K. Wang and Q. Wang, Reversible engineering of cell membrane receptors based on host-guest recognition for on-demand regulation of cellular behavior, *J. Controlled Release*, 2025, **382**, 113701.

43 X. Wu, H. Liu, D. Han, B. Peng, H. Zhang, L. Zhang, J. Li, J. Liu, C. Cui, S. Fang, M. Li, M. Ye and W. Tan, Elucidation and Structural Modeling of CD71 as a Molecular Target for Cell-Specific Aptamer Binding, *J. Am. Chem. Soc.*, 2019, **141**(27), 10760–10769.